CrystEngComm

ROYAL SOCIETY OF CHEMISTRY

PAPER

View Article Online
View Journal | View Issue

Cite this: *CrystEngComm*, 2025, **27**, 7834

Anisotropic conductivity in brownmillerite-type $Ca_2Fe_2O_5$ observed by measurements on oriented floating-zone grown single crystals

Esther M. Curtis, [a] Josie E. Auckett[ab] and Ivana Radosavljević Evans *[a]

Received 1st October 2025,
Accepted 9th November 2025

DOI: 10.1039/d5ce00949a

rsc.li/crystengcomm

Brownmillerite-type $Ca_2Fe_2O_5$ is a mixed ionic and electronic conductor with applications as an electrode material for solid oxide fuel cells and solid oxide electrolyser cells. Long-range oxide ion migration in $Ca_2Fe_2O_5$ has been computationally predicted to be predominantly two-dimensional, restricted to the (*ac*) crystallographic plane. We have used the floating zone method to grow large high-quality single crystals of $Ca_2Fe_2O_5$ and determine its conductivity on two differently oriented single crystal samples in order to directly probe the anisotropy of transport properties. Impedance spectroscopy measurements have shown the conductivity in the (*ac*)-plane to be up to one and a half order of magnitude higher than that parallel to the crystallographic *b*-axis. This degree of anisotropy of the conductivity is higher than that observed experimentally in most other oxide ion or mixed conductors belonging to the apatite and melilite structural family, highlighting the suitability of brownmillerite-type materials for applications in devices requiring components in oriented crystal or thin-film forms.

Introduction

$Ca_2Fe_2O_5$ is a mixed ionic and electronic conductor with applications in solid oxide fuel cells (SOFCs) and solid oxide electrolyser cells (SOECs). Recent studies on $Ca_2Fe_2O_5$ derivatives have shown that they can be used for the air electrode in SOECs, with $Ca_2Fe_{0.8}Co_{1.2}O_5$ and $Ca_2Fe_{1.95}Mg_{0.05}O_5$ having area specific resistances of 0.29 Ω cm^2 at 700 °C and 0.17 Ω cm^2 at 800 °C, respectively.[1,2] Furthermore, Co-doped $Ca_2Fe_2O_5$ has been demonstrated to be a cathode material for SOFCs[3,4] and studies of $Ca_2Fe_2O_5$ as an electrode material for Li ion batteries have been carried out.[1,5–7] A deeper understanding of the anisotropic nature of ionic conductivity in $Ca_2Fe_2O_5$ could allow for a tuning of the ionic contribution of the conductivity in applications utilising oriented thin films, similar to tuning conductivity in thin films using strain engineering.[8–10]

$Ca_2Fe_2O_5$ adopts the layered brownmillerite-type structure. Brownmillerite-type materials have a general formula $A_2B_2O_5$ and can be described as oxygen-deficient perovskites ($A_2B_2O_6$) where one sixth of the oxygen atoms are replaced by ordered vacancies. The structure consists of alternating layers of corner-sharing BO_6 octahedra and BO_4 tetrahedra, such that the inter-layer and intra-layer ordering of the tetrahedra connected into chains determines the space group adopted by the material. The Ca^{2+} cations are located on the sites between the layers. At room-temperature, $Ca_2Fe_2O_5$ crystallises in space group *Pnma*, with tetrahedral chains strictly ordered (Fig. 1). Around 700 °C, it undergoes a phase transition to an incommensurately-modulated phase, *Imma*(00γ)s00,[11–14] followed by two further phase transitions at 1100 °C and 1300 °C.[15] $Ca_2Fe_2O_5$ melts congruently at 1447 °C.[16]

Transport properties of a number of brownmillerite-type materials have been reported in the literature. $Ba_2In_2O_5$ is a modest oxide ion conductor before it transforms into a cubic disordered perovskite phase; its total conductivity is 9.6×10^{-5} S cm^{-1} at 600 °C, but reaches 0.1 S cm^{-1} at 1100 °C.[17] $Sr_2Fe_2O_5$ is a mixed conductor with oxide ion conductivity of 0.22 S cm^{-1} at 900 °C, above the structural phase transition to a disordered cubic perovskite phase.[18,19] The anisotropic oxide ion migration in the brownmillerite form of $Sr_2Fe_2O_5$ has been described in computational studies by both classical and *ab initio* molecular dynamics (AIMD), while in the high temperature form the material has a three-dimensional network of equivalent oxide ion migration pathways.[20–23] $Ca_2Fe_2O_5$ is also a mixed conductor with oxide ion conductivity of 4×10^{-3} S cm^{-1} at 900 °C.[24] A number of chemical modifications have been attempted in order to raise its conductivity, *e.g.* partial substitution of Fe^{3+} by Al^{3+}, Mn^{4+}, Co^{3+} and Ga^{3+} cations.[25–29] Only Co-doped $Ca_2Fe_2O_5$ was

[a] *Department of Chemistry, Durham University, Lower Mountjoy, South Road, Durham, DH1 3LE, UK. E-mail: ivana.radosavljevic@durham.ac.uk*
[b] *Australian Synchrotron, ANSTO, 800 Blackburn Road, Clayton, VIC 3168, Australia*

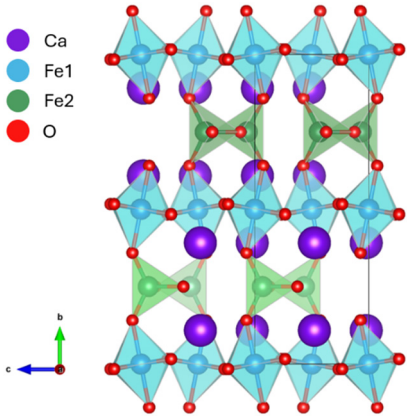

Fig. 1 The room-temperature structure of $Ca_2Fe_2O_5$ showing FeO_4 tetrahedra (green), FeO_6 octahedra (blue), Ca atoms (purple) and O atoms (red).

found to have a higher total conductivity (5.6 S cm^{-1} at 900 °C) compared to $Ca_2Fe_2O_5$ (total conductivity of 0.56 S cm^{-1} at 900 °C) and other brownmillerite-type mixed conductors.[28] The layered structure of $Ca_2Fe_2O_5$ (Fig. 1), in particular the intrinsic vacancies concentrated in the (*ac*)-plane suggest that ionic migration in this material could be anisotropic. This has also been computationally predicted, albeit without being quantified.[22,30] In order to directly demonstrate and quantify the anisotropic nature of conductivity, measurements on oriented single crystal samples need to be performed. This has been reported for a small number of apatite-type $(Ln_{9.33}(XO_4)_6O_2$, Ln = La, Pr, Sm, Nd; X = Si, Ge and $Nd_{(28+x)/3}Al_xSi_{6-x}O_{26}$, x = 0, 1, 2)[31–36] and melilite-type $([La_{1+x}Ca_{1-x}]_2[Ga]_2[Ga_2O_{7+x/2}]_2$, $0.1 \leq x \leq 0.6$)[37] materials. In addition, the oxide ion diffusivity and surface exchange was measured on oriented single crystals of A_2NiO_4 (A = Nb, La, Pr).[38,39]

In this study, we experimentally demonstrated the highly anisotropic nature of oxide ion conductivity in $Ca_2Fe_2O_5$ by conductivity measurements on oriented single crystals. We grew large, high-quality single crystals of $Ca_2Fe_2O_5$ using the floating-zone (FZ) method. Oriented samples were characterised using Laue X-ray diffraction, and conductivity was measured by impedance spectroscopy both parallel to the *b*-axis and within the (*ac*)-plane. These measurements showed that oxide ion conductivity in $Ca_2Fe_2O_5$ is predominantly two-dimensional, occurring preferentially within the layers containing the FeO_4 tetrahedral groups.

Experimental

Synthesis of polycrystalline $Ca_2Fe_2O_5$

20 g of polycrystalline $Ca_2Fe_2O_5$ were prepared by conventional solid-state synthesis. $CaCO_3$ (≥99.0%, Sigma-Aldrich) and Fe_2O_3 (≥99%, Sigma-Aldrich) were dried overnight (400 °C, 12 h) and stoichiometric amounts were weighed out. The powder mixture was ground, pressed into 13 mm diameter pellets and fired at 1100 °C for 36 h. After firing, the powder was ball milled (300 rpm, 30 min) and powder X-ray diffraction (PXRD) was utilised to confirm phase purity.

Floating-zone crystal growth

To prepare the feed and seed rods, $Ca_2Fe_2O_5$ powder was packed into rubber tubes, evacuated, and pressed at 40 MPa using a hydrostatic press to give suitable rods for single crystal growth. The rods were sintered (1200 °C, 12 h) to increase their density. The sintered rods had an approximate diameter of 4.5 mm and lengths between 4–6 cm. A Crystal Systems Corporation optical FZ furnace (model FZ-T-10000-H-VII-VPO-PC) equipped with four 300 W halogen lamps was used for single crystal growth. The growth atmosphere was 20 : 80 O_2 : Ar flowing at 0.5 L min^{-1}. The $Ca_2Fe_2O_5$ feed rod was pre-melted in the FZ furnace to reduce bubble formation in the molten zone during the growth,[40] by passing the feed rod through the lamp focus at 20 mm h^{-1}, with the feed and seed rods counter-rotated at 30 rpm. Subsequently, single crystal of $Ca_2Fe_2O_5$ was grown using the pre-melted feed rod at 1 mm h^{-1}, with the feed and seed rods counter-rotated (30 rpm). A lamp power of ~58% was required. The tip of the pre-melted feed rod was cleaved off and used as the seed. Once the molten zone was formed, the growth proceeded in a controlled manner for 48 h, requiring no manual interference.

Orientation and cutting of single crystal $Ca_2Fe_2O_5$

To prepare oriented $Ca_2Fe_2O_5$ single crystals for impedance measurements, the whole crystal was mounted in Crystalbond 509-3 resin and cut using a Logitech Model 15 diamond wire saw. Excess resin remaining on the cut slices was removed with acetone. Single crystal slices for conductivity measurements were cut from the final 2 cm of the crystal grown. Laue patterns were collected on these faces using a Real-Time Back-Reflection Laue Camera (Multiwire Laboratories Model MWL12). The Laue patterns were indexed using the NorthStar7.0 software and compared to a simulated Laue pattern for $Ca_2Fe_2O_5$, generated in the program WinLaue. These Laue patterns confirmed that the slice for measurements parallel to the *b*-axis had been cut with the faces (where the electrodes would be applied) indexed as the (010) plane, and the slice for measurements within the (*ac*)-plane had been cut with the faces (where the electrodes would be applied) indexed as the (101) plane.

Powder X-ray diffraction

PXRD patterns were collected on a Bruker D8 Advance diffractometer with a Lynx-Eye PSD detector and Cu Kα radiation (λ = 1.5406 Å). All PXRD patterns used to monitor the progress of the solid-state reaction were collected at room temperature in the 2θ range 10–90° with a data collection time of 20–30 minutes. The pattern of the final polycrystalline sample was collected at room temperature in the 2θ range 10–120° with a data collection time of 10 hours.

Variable temperature X-ray diffraction patterns were recorded in 20 °C intervals on heating (50–990 °C) and cooling (980–40 °C). An Anton Parr HTK1200 high-temperature attachment was used, and the furnace temperature was calibrated with an external alumina standard. Patterns were recorded over a 2θ range of 10–120° with a collection time of an hour at each temperature. The resulting diffraction patterns were analysed by sequential Rietveld fitting.

All diffraction data were analysed using the Rietveld method[41] implemented in the TOPAS Academic software.[42,43] Refined parameters included unit-cell parameters, a single isotropic atomic displacement parameter, sample displacement parameter, background polynomial terms and pseudo-Voigt peak shape function terms.

Single crystal X-ray diffraction

Single crystal X-ray diffraction data were collected on a Bruker D8 VENTURE diffractometer, using an ImS-microsource, Mo Kα radiation (λ = 0.7107 Å) and a PHOTON III C7 MM CPAD detector. An Oxford Cryosystems Cryostream 700+ was used to cool the sample to 120 K. Data reduction was carried out in Apex5 software, including a multi-scan absorption correction with an additional spherical absorption correction, reducing R_{int} from 18% to 9%. The structure refinement was performed in Jana2006 (ref. 44 and 45) using the published structure of $Ca_2Fe_2O_5$ as a starting model.[14] The atomic positions and anisotropic atomic displacement parameters for all atoms were refined. All structure visualisation was carried out in the VESTA software.[46]

Impedance spectroscopy

Impedance spectroscopy data on polycrystalline $Ca_2Fe_2O_5$ were collected on a 10 mm diameter pellet sintered at 1200 °C for 12 h, with a relative density of 89%. Data were also collected on the FZ grown single crystal samples of $Ca_2Fe_2O_5$ oriented to measure parallel to the *b*-axis or in the (*ac*)-plane. The indexed (010) or (101) faces, respectively, of the oriented single crystal slices, and the flat faces of the sintered pellets, were coated with platinum ink (Melator Technologies) for use as electrodes. The samples were mounted on a Probostat A-6 cell and the electrodes were fired at 1000 °C for 30 min. Impedance measurements were carried out in air and dry N_2 in 20 °C intervals between 200–1000 °C with a ramp rate of 2 °C min^{-1} and a frequency range of 10^{-1}–10^{7} Hz. Data were analysed by simple circuit fitting using the ZView/Zplot software (Scribner Associates).

Results and discussion

Powder X-ray diffraction of $Ca_2Fe_2O_5$

PXRD patterns collected on the powder used for crystal growth were fitted using the brownmillerite structural model in space group *Pnma*.[14] An excellent fit was obtained with no peaks unaccounted for, confirming the phase purity. The agreement factor R_{wp} = 6.01% was achieved, and the final Rietveld fit obtained is shown in Fig. 2.

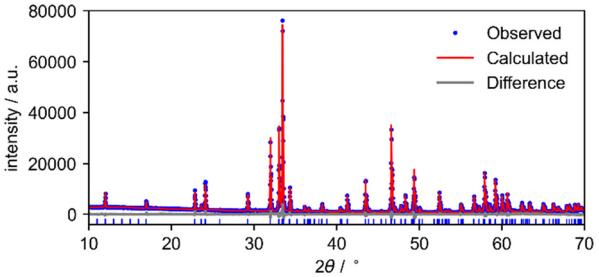

Fig. 2 Rietveld fit of the PXRD pattern of polycrystalline $Ca_2Fe_2O_5$ used to prepare the feed and seed rods. The blue, red and grey curves show the observed pattern, calculated pattern and the difference curve, respectively.

Variable temperature PXRD data collected on $Ca_2Fe_2O_5$ between 40 °C and 990 °C were analysed by sequential Rietveld refinement, using the brownmillerite structural model in space group *Pnma*. The temperature evolution of the unit cell parameters is shown in Fig. 3 and a surface plot of the diffraction data from which this dependence was extracted is given in Fig. S1. A subtle change of slope can be seen at around ~400 °C. The onset of oxide ion mobility in $Ca_2Fe_2O_5$ has been observed by $^{18}O/^{16}O$ isotope exchange reactions to occur from 477 °C,[22] and this is presumably related to the subtle change of slope in the unit cell parameter trends observed from our X-ray diffraction data at around 400 °C, as well as in the changes of slope in the Arrhenius conductivity curves (*vide infra*). Similarly subtle changes in unit cell parameters as a function of temperature were correlated with similar changes in properties in

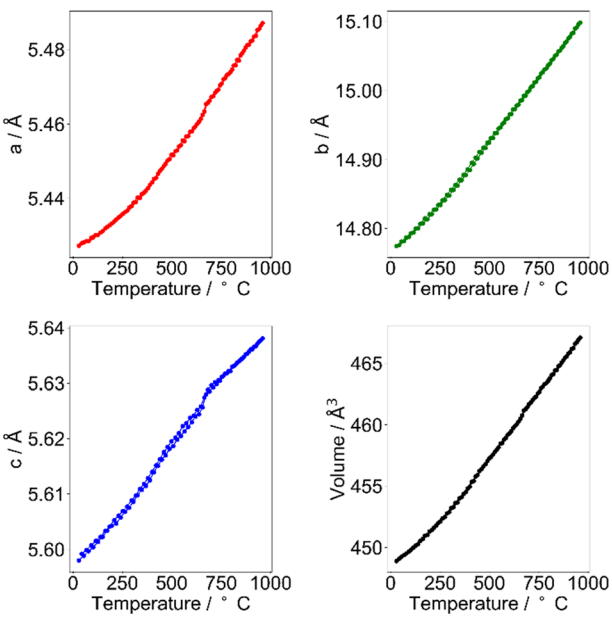

Fig. 3 The variation of the unit cell parameters as a function of temperature (heating and cooling). Error bars are smaller than the data markers.

brownmillerite-type Sr_2ScGaO_5.[47] The temperature evolution of the *a* and *c* unit cell parameters (red and blue curves in Fig. 3) shows a small discontinuity and change in slope at 670 °C, coinciding with the structural phase transition to the *Imma*(00γ)s00 phase, where the incommensurate modulation is related to the tetrahedral chain ordering within the (*ac*)-plane.[11,12,15]

Oriented single crystals of $Ca_2Fe_2O_5$

The crystal obtained by the FZ growth was cylindrical with a length of 6.5 cm and a diameter of 0.4 cm (Fig. 4). The last 3.5 cm of the crystal had large facets on opposite sides along the length of the crystal, previously attributed to the (*ac*)-plane using Laue diffraction.[40] No visible grain boundaries were observed on the outside of the crystal past the first 0.5 cm of growth, with the relatively quick FZ domain selection process attributed to the use of the cleaved tip of the pre-melted feed as the seed.[40] To confirm the crystal quality, a small fragment (10^{-4} mm^3) of the large single crystal was characterised by single crystal X-ray diffraction. The structure was refined with unit cell parameters *a* = 5.4188(4), *b* = 14.7045(9), *c* = 5.5866(4) and space group *Pnma*, with further crystallographic data given in Table 1 and the structure shown in Fig. 1. Furthermore, a section of the single crystal was ground and PXRD was collected, and a good fit was obtained with an agreement factor R_{wp} = 9.31%. The Rietveld fit is given in Fig. S2. Single-domain slices of $Ca_2Fe_2O_5$ from the FZ grown crystal were subsequently prepared and X-ray Laue back reflection patterns collected on the faces (Fig. 5). The sample oriented with the flat faces perpendicular to the *b*-axis (used to measure conductivity along the *b*-axis) is indexed with the (010) reflection almost in the centre of the pattern; this confirms that the faces are the (010) plane. The sample cut to measure conductivity within the (*ac*)-plane is indexed with the (101) reflection near the centre of the Laue pattern and the faces were confirmed to be the (101) plane. The sharp, distinct reflections present in the Laue patterns also confirm that the crystal quality is sufficient for conductivity measurements. The single domain nature of the sample was confirmed by collecting multiple Laue patterns across the surface of the crystal; these were identical at all points on the surface.

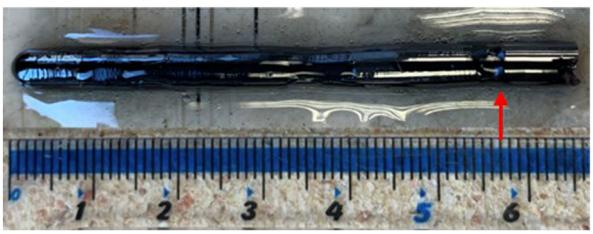

Fig. 4 The $Ca_2Fe_2O_5$ crystal mounted in resin in preparation of cutting with a diamond wire saw. The scale bar is in centimetres. The red arrow marks the seeding point.

Table 1 The crystallographic parameters from the structure refinement carried out on a crystal of $Ca_2Fe_2O_5$ grown by the FZ method

Unit cell parameters	
Space group	*Pnma*
a	5.4188(4)
b	14.7045(9)
c	5.5866(4)
V	445.1(1)
Number of reflections	
All	11 961
Observed	6138
Merged	759
Number of refined parameters	46
R_{sym}/%	8.06
R/%	3.55
w*R*/%	2.69

Transport properties

Impedance spectroscopy data were recorded on a sintered pellet of $Ca_2Fe_2O_5$ and the two oriented single crystal slices to compare the conductivity in a polycrystalline sample with that parallel to the *b*-axis and within the (*ac*)-plane. Complex plane plots for all three samples show a single semicircular response at low temperatures. The capacitance was calculated from the apex of the arc using the RC time constant relationship $1/\omega = RC$.[48–50] The capacitance was used to attribute the response to a grain boundary response for the polycrystalline pellet (10^{-10}–10^{-8} F) or a surface response for the single crystal samples (10^{-11}–10^{-9} F).[48] In all cases, the electrode response is flat at low temperatures, suggesting dominant electronic conductivity.[50] At higher temperatures (above ~500 °C), a Warburg response is observed, indicative of the ionic conductivity contribution.[48] The total resistivity was estimated as the high intercept of the semicircular response. With increasing temperature, the grain boundary and surface responses disappeared, and above 318 °C, only the electrode response remained for all samples. In this region, the total resistivity was estimated as the high frequency intercept of the electrode response. Nyquist plots of the polycrystalline sample are given in Fig. S3.

Fig. 6 shows the total conductivity of oriented single crystal samples of $Ca_2Fe_2O_5$, probing the properties within the (*ac*)-plane and along the *b*-axis, and that of the polycrystalline sample for comparison. The activation energy values calculated in three temperature regions (<460 °C, 460–650 °C, >700 °C) using the Arrhenius relationship given in eqn (1), where σ is the conductivity, σ_0 a preexponential constant, E_a the activation energy, *T* the temperature and *R* the ideal gas constant.

$$\sigma = \left(\frac{\sigma_0}{T}\right) e^{-\frac{E_a}{RT}} \quad (1)$$

The activation energies are given in Table 2. The onset of oxide ion mobility, observed by $^{18}O/^{16}O$ isotope exchange reactions, was reported by Paulus *et al.* to occur above 477 °C.[22] Hence, the changes of slope around 460 °C seen in all conductivity curves in Fig. 6 can therefore be

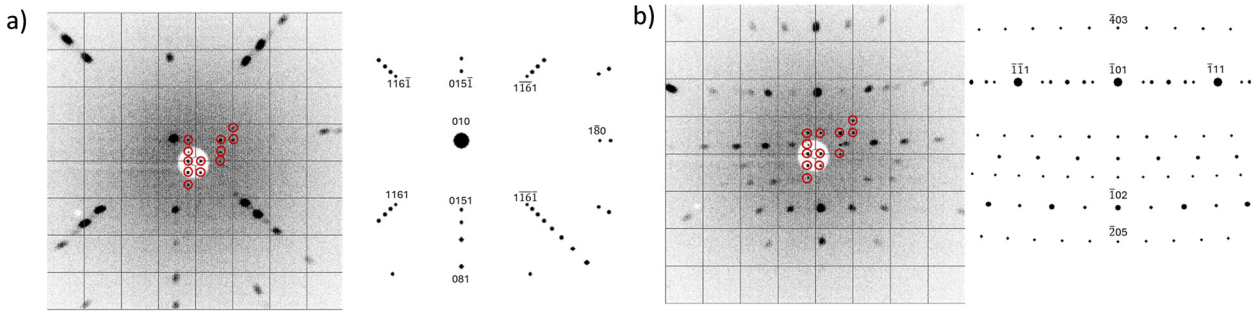

Fig. 5 The Laue patterns collected on the flat surfaces of the $Ca_2Fe_2O_5$ single crystal slices (left) and simulated Laue patterns used to confirm indexing (right). a) The sample used for oriented conductivity measurements parallel to the *b*-axis and b) the sample used for oriented conductivity measurements within the (*ac*)-plane. The small square-shaped markings, circled in red, near the central beam hole in both images are detector artifacts.

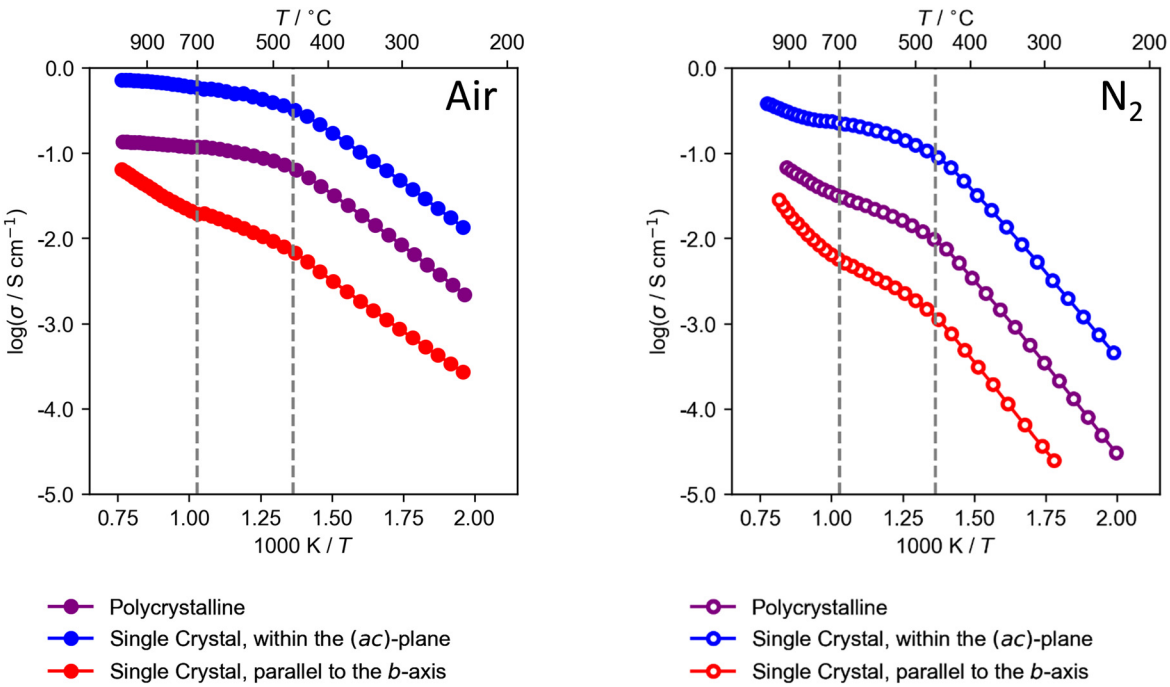

Fig. 6 Arrhenius plots of the conductivity of $Ca_2Fe_2O_5$ measured on a polycrystalline sample (purple) and two single-crystal samples, oriented to measure conductivity parallel to the *b*-axis (red) and in the (*ac*)-plane (blue). Data collection was carried out in air (left) and flowing nitrogen (right). The dashed grey lines separate the three temperature regions for which the activation energies were calculated.

attributed to the contribution of this new process to the total conductivity. Furthermore, subtle change in the slope of the temperature dependence of the unit cell parameters around 400 °C, observed in our X-ray diffraction data (Fig. 3), suggests that structural changes they reflect are related to this new process contributing to the total conductivity. Further changes of slope particularly notable in the *b*-direction, occur at 700 °C, the temperature of the phase transition of $Ca_2Fe_2O_5$ to an incommensurately modulated *Imma*(00γ)s00 structure.[11,12] This phase transition introduces aperiodic ordering of the tetrahedral chains in the layers parallel to the (*ac*)-plane, which likely makes the exchange of oxide ions between these layers and the apical sites in the octahedral layers, observed in AIMD simulations by Paulus *et al.*,[22] less facile, leading to pronounced increase in the activation energy along the *b*-direction. Impedance spectroscopy data collected in dry N_2 show a lower total conductivity for all samples. This provides evidence for the p-type electronic conductivity in $Ca_2Fe_2O_5$,[24] with the lower oxygen partial pressure suppressing the electronic part of the conductivity. Above the phase transition to the incommensurate structure, the total conductivity measured in the two atmospheres starts to converge, indicating a diminishing contribution of electronic conductivity with increasing temperature. Transference numbers show an increase in the ionic component of the conductivity with increasing temperature, especially above the phase transition (Table 3). Similar behaviour has been

Table 2 The activation energies of $Ca_2Fe_2O_5$ calculated in three different regions: below 460 °C, between 460–650 °C and above 700 °C. These were calculated for single crystal samples measured parallel to the *b*-axis, within the (*ac*)-plane, and a polycrystalline sample. Activation energies were calculated for data collected in both air and dry N_2

		Activation energies/eV		
Temperature/°C		Single crystal, parallel to the *b*-axis	Single crystal, within the (*ac*)-plane	Polycrystalline
<460	Air	0.501(6)	0.548(4)	0.54(3)
	N_2	0.85(2)	0.835(1)	0.84(7)
460–650	Air	0.37(1)	0.235(4)	0.25(2)
	N_2	0.44(4)	0.32(1)	0.38(10)
>700	Air	0.53(2)	0.164(4)	0.151(5)
	N_2	0.7(1)	0.27(2)	0.4(1)

Table 3 The transference numbers of $Ca_2Fe_2O_5$ calculated from conductivity data collected in air and N_2

	t_{ion}/%		
Temperature/°C	Polycrystalline	(*ac*)-Plane	*b*-Axis
300	3.7(7)	10.4(9)	2.5(4)
400	10(1)	23(2)	6.3(6)
500	18(1)	32(2)	10.2(5)
600	24(2)	36(1)	11.6(9)
700	32(2)	38(1)	14(1)
800	41(4)	38(2)	16.5(8)

reported for other ferrite mixed ionic and electronic conductors such as $Sr_4Fe_6O_{13}$ and $Gd_3Fe_5O_{12}$.[51,52]

Directionality of oxide ion diffusion in $Ca_2Fe_2O_5$

The diffusion mechanism of oxide ions in $Ca_2Fe_2O_5$ has been modelled by AIMD simulations, predicting long-range oxide ion diffusion predominantly within the (*ac*)-plane.[22] AIMD simulations at temperatures above 797 °C show a zigzag-to-zagzig switching of the orientation of the tetrahedral chains in $Ca_2Fe_2O_5$ occurring on the picosecond time-scale.[22] At these temperatures, the apical oxide ions within the octahedral layers start migrating into the oxygen vacancies within the tetrahedral layers.[22] A study of $Ca_2Fe_2O_5$ thin films reduction into quasi-2D layered $CaFeO_2$ (ref. 30) showed that the reduction of the *b*-axis-oriented film took about four times longer than of the film oriented perpendicular to this direction. Since it was assumed that oxygen was lost predominantly from the face of the film, it was proposed that long-range oxide ion diffusion within $Ca_2Fe_2O_5$ occurred predominantly within the (*ac*)-plane of the brownmillerite structure; however, the degree of anisotropy could not be quantified.

Through impedance spectroscopy measurements on oriented single crystal samples of $Ca_2Fe_2O_5$, we demonstrated experimentally that the total conductivity within the (*ac*)-plane is up to one and a half orders of magnitude higher than that parallel to the *b*-axis (Fig. 6). The trends in conductivity between the samples are maintained above the phase transition into the incommensurately modulated structure; this is expected, as the high temperature $Ca_2Fe_2O_5$ retains the layers present in the low temperature form.[11,12,14,40] Previous studies of apatite-type materials $(Ln_{9.33}(XO_4)_6O_2$, Ln = La, Pr, Sm, Nd; X = Si, Ge and $Nd_{(28+x)/3}Al_xSi_{6-x}O_{26}$ for x = 0, 1, 2) and melilite-type $[La_{1+x}Ca_{1-x}]_2[Ga]_2[Ga_2O_{7+x/2}]_2$ show an increase of around half an order of magnitude in most cases, with only $La_{9.33}(SiO_4)_6O_2$ displaying a higher anisotropy of conductivity, of up to two orders of magnitude.[31–37]

Conclusions

Centimetre-sized high-quality single crystals of $Ca_2Fe_2O_5$ were grown by the floating zone method and two differently oriented samples were prepared. The quality and orientation of the single crystals were confirmed using X-ray Laue diffraction. Impedance spectroscopy measurements were carried out on the oriented single crystals to probe the conductivity within the (*ac*)-plane and parallel to the *b*-axis, and additionally on a polycrystalline sample as a reference. Our study experimentally demonstrates that long-range oxide ion diffusion in brownmillerite-type $Ca_2Fe_2O_5$ occurs predominantly in the (*ac*)-plane, consistent with theoretical predictions based on *ab initio* molecular dynamics simulations.[20–23] The transport properties exhibit a significant degree of anisotropy, with the total conductivity measured within the (*ac*)-plane found to be up to one and a half orders of magnitude higher than that parallel to the *b*-axis. This suggests that $Ca_2Fe_2O_5$ is a good candidate for solid state electrochemistry applications where thin films or oriented single crystals are required.

Conflicts of interest

There are no conflicts to declare.

Data availability

Data supporting this article are available at https://doi.org/10.15128/r2j9602067k and in the supplementary information (SI) document.

Supplementary information is available. See DOI: https://doi.org/10.1039/d5ce00949a.

Acknowledgements

The authors thank the Leverhulme Trust for the provision of a PhD research project grant for EMC (RPG-2023-080). IRE thanks Durham University for research leave.

Notes and references

1 E. Squizzato, G. Carollo and A. Glisenti, *Int. J. Hydrogen Energy*, 2021, **46**, 24555–24566.
2 S. J. Lee, S. M. Yong, D. S. Kim and D. K. Kim, *Int. J. Hydrogen Energy*, 2012, **37**, 17217–17224.
3 V. Cascos, R. Martínez-Coronado, J. A. Alonso and M. T. Fernández-Díaz, *Int. J. Hydrogen Energy*, 2015, **40**, 5456–5468.
4 Baijnath, P. Tiwari and S. Basu, *Int. J. Hydrogen Energy*, 2019, **44**, 10059–10070.
5 S. K. Sundriyal and Y. Sharma, *Appl. Surf. Sci.*, 2021, **560**, 150055.
6 P. Zhu, G. Yang, X. Sun, Q. Cao, Y. Zhao, R. Ding, E. Liu and P. Gao, *New J. Chem.*, 2023, **47**, 11102–11109.
7 G. Spanu, A. Celeste, F. Bozza, E. Serra, P. Torelli, L. Braglia, S. Brutti, P. Reale and L. Silvestri, *Batteries Supercaps*, 2024, **7**, e202400063.
8 G. Yang, M. El Loubani, H. R. Chalaki, J. Kim, J. K. Keum, C. M. Rouleau and D. Lee, *ACS Appl. Electron. Mater.*, 2023, **5**, 4556–4563.
9 P. Arunkumar, R. Ramaseshan, S. Dash and K. S. Babu, *Sci. Rep.*, 2017, **7**, 3450.
10 P. Arunkumar, P. Panda, M. Sribalaji, R. Ramaseshan, A. K. Keshri and K. S. Babu, *Electrochim. Acta*, 2017, **240**, 437–446.
11 H. Krüger and V. Kahlenberg, *Acta Crystallogr., Sect. B: Struct. Sci.*, 2005, **61**, 656–662.
12 H. Krüger, V. Kahlenberg, V. Petříček, F. Phillipp and W. Wertl, *J. Solid State Chem.*, 2009, **182**, 1515–1523.
13 T. Labii, M. Ceretti, A. Boubertakh, W. Paulus and S. Hamamda, *J. Therm. Anal. Calorim.*, 2013, **112**, 865–870.
14 P. Berastegui, S.-G. Eriksson and S. Hull, *Mater. Res. Bull.*, 1999, **34**, 303–314.
15 E. Asenath-Smith, S. Misture and D. Edwards, *J. Solid State Chem.*, 2011, **184**, 2167–2177.
16 S. Cheng, E. Nekhoroshev, M. Shevchenko, D. Shishin and E. Jak, *Ceram. Int.*, 2024, **50**, 45438–45452.
17 J. B. Goodenough, J. E. Ruiz-Diaz and Y. S. Zhen, *Solid State Ion.*, 1990, **44**, 21–31.
18 I. A. Leonidov, M. V. Patrakeev, J. A. Bahteeva, K. V. Poholok, D. S. Filimonov, K. R. Poeppelmeier and V. L. Kozhevnikov, *J. Solid State Chem.*, 2006, **179**, 3045–3051.
19 M. Schmidt and S. J. Campbell, *J. Solid State Chem.*, 2001, **156**, 292–304.
20 S. Ambaum, N. L. Allan, R. Dittmann and R. A. De Souza, *Chem. Mater.*, 2024, **36**, 2039–2048.
21 J. E. Auckett, W. T. Lee, K. C. Rule, A. Bosak and C. D. Ling, *Inorg. Chem.*, 2019, **58**, 12317–12324.
22 W. Paulus, H. Schober, S. Eibl, M. Johnson, T. Berthier, O. Hernandez, M. Ceretti, M. Plazanet, K. Conder and C. Lamberti, *J. Am. Chem. Soc.*, 2008, **130**, 16080–16085.
23 J. E. Auckett, A. J. Studer, E. Pellegrini, J. Ollivier, M. R. Johnson, H. Schober, W. Miiller and C. D. Ling, *Chem. Mater.*, 2013, **25**, 3080–3087.
24 A. L. Shaula, Y. V. Pivak, J. C. Waerenborgh, P. Gaczyński, A. A. Yaremchenko and V. V. Kharton, *Solid State Ionics*, 2006, **177**, 2923–2930.
25 Q. E. Stahl, G. J. Redhammer, G. Tippelt and A. Reyer, *Phys. Chem. Miner.*, 2019, **46**, 271–298.
26 R. K. Hona, A. Huq and F. Ramezanipour, *Mater. Chem. Phys.*, 2019, **238**, 121924.
27 R. K. Hona, A. Huq and F. Ramezanipour, *Ionics*, 2019, **25**, 1315–1321.
28 A. L. Shaula, A. A. Markov, E. N. Naumovich, J. C. Waerenborgh, Y. V. Pivak and V. V. Kharton, *Solid State Ionics*, 2012, **225**, 206–210.
29 V. V. Kharton, I. P. Marozau, N. P. Vyshatko, A. L. Shaula, A. P. Viskup, E. N. Naumovich and F. M. B. Marques, *Mater. Res. Bull.*, 2003, **38**, 773–782.
30 S. Inoue, M. Kawai, N. Ichikawa, H. Kageyama, W. Paulus and Y. Shimakawa, *Nat. Chem.*, 2010, **2**, 213–217.
31 S. Nakayama and M. Highchi, *J. Mater. Sci. Lett.*, 2001, **20**, 913–915.
32 S. Nakayama, M. Sakamoto, M. Higuchi, K. Kodaira, M. Sato, S. Kakita, T. Suzuki and K. Itoh, *J. Eur. Ceram. Soc.*, 1999, **19**, 507–510.
33 M. Higuchi, K. Kodaira and S. Nakayama, *J. Cryst. Growth*, 2000, **216**, 317–321.
34 S. Nakayama and M. Sakamoto, *Solid State Ionics*, 2013, **253**, 47–52.
35 T. An, T. Baikie, F. Wei, S. S. Pramana, M. K. Schreyer, R. O. Piltz, J. F. Shin, J. Wei, P. R. Slater and T. J. White, *Chem. Mater.*, 2013, **25**, 1109–1120.
36 Y. Masubuchi, M. Higuchi, S. Kikkawa, K. Kodaira and S. Nakayama, *Solid State Ionics*, 2004, **175**, 357–360.
37 F. Wei, H. Gasparyan, P. J. Keenan, M. Gutmann, Y. Fang, T. Baikie, J. B. Claridge, P. R. Slater, C. L. Kloc and T. J. White, *J. Mater. Chem. A*, 2015, **3**, 3091–3096.
38 J. M. Bassat, M. Burriel, O. Wahyudi, R. Castaing, M. Ceretti, P. Veber, I. Weill, A. Villesuzanne, J. C. Grenier, W. Paulus and J. A. Kilner, *J. Phys. Chem. C*, 2013, **117**, 26466–26472.
39 J. M. Bassat, P. Odier, A. Villesuzanne, C. Marin and M. Pouchard, *Solid State Ionics*, 2004, **167**, 341–347.
40 J. E. Auckett, A. J. Studer and C. D. Ling, *Aust. J. Chem.*, 2014, **67**, 1824–1828.
41 H. M. Rietveld, *J. Appl. Crystallogr.*, 1969, **2**, 65.
42 R. E. Dinnebier, A. Leineweber and J. S. O. Evans, *Rietveld Refinement: Practical Powder Diffraction Pattern Analysis using TOPAS*, De Gruyter, 2010.
43 A. A. Coelho, J. Evans, I. Evans, A. Kern and S. Parsons, *Powder Diffr.*, 2011, **26**, S22.
44 V. Petříček, L. Palatinus, J. Plášil and M. Dušek, *Z. Kristallogr. - Cryst. Mater.*, 2023, **238**, 271–282.
45 V. Petříček, M. Dušek and L. Palatinus, *Z. Kristallogr. - Cryst. Mater.*, 2014, **229**, 345–352.
46 K. Momma and F. Izumi, *J. Appl. Crystallogr.*, 2008, **41**, 653–658.

47 C. A. Fuller, Q. Berrod, B. Frick, M. R. Johnson, S. J. Clark, J. S. O. Evans and I. R. Evans, *Chem. Mater.*, 2019, **31**, 7395–7404.
48 J. T. S. Irvine, D. C. Sinclair and A. R. West, *Adv. Mater.*, 1990, **2**, 132–138.
49 *Impedance Spectroscopy Theory, Experiment and Applicatons*, ed. E. Barsoukov and J. R. Macdonald, Wiley-Interscience, New Jersey, 2nd edn, 2005.
50 A. Ch. Lazanas and M. I. Prodromidis, *ACS Meas. Sci. Au*, 2023, **3**, 162–193.
51 V. V. Kharton, A. L. Shaula, E. N. Naumovich, N. P. Vyshatko, I. P. Marozau, A. P. Viskup and F. M. B. Marques, *J. Electrochem. Soc.*, 2003, **150**, J33–J42.
52 M. Y. Avdeev, M. V. Patrakeev, V. V. Kharton and J. R. Frade, *J. Solid State Electrochem.*, 2002, **6**, 217–224.